

**PCCP****Origin of Fast Oxide Ion Diffusion along Grain Boundaries in Sr-doped LaMnO<sub>3</sub>**

Journal:	<i>Physical Chemistry Chemical Physics</i>
Manuscript ID	CP-ART-04-2018-002443.R2
Article Type:	Paper
Date Submitted by the Author:	29-Jun-2018
Complete List of Authors:	Polfus, Jonathan; SINTEF Industry, Sustainable Energy Technology Yildiz, Bilge; Massachusetts Institute of Technology, Tuller, Harry; Massachusetts Institute of Technology, Department of Materials Science and Engineering

SCHOLARONE™  
Manuscripts

# Origin of Fast Oxide Ion Diffusion along Grain Boundaries in Sr-doped $\text{LaMnO}_3$

Jonathan M. Polfus<sup>a,b,\*</sup>, Bilge Yildiz<sup>b,c</sup>, Harry L. Tuller<sup>b</sup>

<sup>a</sup>SINTEF Industry, Sustainable Energy Technology, PO Box 124 Blindern, NO-0314 Oslo, Norway

<sup>b</sup>Department of Materials Science and Engineering, <sup>c</sup>Department of Nuclear Science and Engineering, Massachusetts Institute of Technology, 77 Massachusetts Avenue, Cambridge, MA 02139, USA

\*Contact email: jonathan.polfus@sintef.no

## Abstract

The prospect of significantly enhanced oxide ion diffusion along grain boundaries in Sr-doped  $\text{LaMnO}_3$  (LSM) was investigated by means of density functional theory calculations applied to a  $\Sigma 5$  (3 1 0)[0 0 1] grain boundary. The structure of the grain boundary was optimized by rigid body translation, and segregation energies were calculated for oxygen vacancies and Sr-acceptors. Two potentially fast diffusion paths were identified along the grain boundary core based on the interconnectivity between neighbouring sites with a strong tendency for segregation of oxygen vacancies. The migration barriers for these paths, obtained with the nudged elastic band method, amounted to about 0.6 eV. Based on the obtained migration barriers and concentrations of oxygen vacancies for the relevant core sites, the grain boundary diffusion coefficient was estimated to be enhanced by 3 to 5 orders of magnitude relative to the bulk in the temperature range 500-900 °C. Space-charge effects were determined to be quite insignificant for the transport properties of LSM grain boundaries.

## 1. Introduction

Acceptor doped perovskite oxides are widely studied for application in solid state electrochemical energy conversion devices such as electrolytes and electrodes in solid oxide fuel cells (SOFC).<sup>1</sup> The acceptor Sr-doped  $\text{LaMnO}_3$  (LSM) is well-established as a SOFC cathode material due to its high electrical conductivity, thermochemical compatibility with yttria-stabilized zirconia (YSZ) electrolytes and appreciable electrocatalytic activity towards the oxygen reduction reaction.<sup>2-7</sup> Nevertheless, cathode activity remains a limiting factor for the overall performance of SOFCs, becoming increasingly important at lower operating temperatures.

The predominating cathode reaction mechanism depends on the electrical and geometrical properties of the cathode material or composite. Due to the limited bulk ionic conductivity of LSM, composite LSM/YSZ cathodes are commonly used in order to increase the active cathode area that is normally limited to the region close to the three-phase boundaries. On the other hand, the bulk reaction path – which proceeds by ionic transport through the cathode – has the potential to drastically improve the cathode performance

since the whole cathode surface becomes active. The bulk path contributes to the overall cathode activity when the cathode material, as a mixed ionic-electronic conductor (MIEC), exhibits sufficient ambipolar transport of oxide ions and electronic charge carriers.

Navickas et al. recently reported a remarkable enhancement of oxygen exchange and diffusion kinetics of grain boundaries in LSM by up to 3 orders of magnitude relative to the bulk by means of oxygen isotope exchange experiments combined with secondary ion mass spectroscopy.<sup>8</sup> Saranya et al. reported even higher enhancements in oxygen diffusivities at LSM grain boundaries of up to six orders of magnitude at 773 K,<sup>9</sup> and enhanced oxygen diffusion has recently also been reported along LSM threading dislocations.<sup>10</sup> Such enhancements in exchange kinetics and diffusion by grain boundary engineering represents a significant opportunity for improved SOFC cathodes. The underlying mechanism associated with the remarkable enhancement in oxygen ion diffusion via grain boundaries remains uncertain, and there are several reasonable possibilities.<sup>11</sup> The low ionic conductivity of LSM can be ascribed to low concentrations – rather than a low mobility – of oxygen vacancies. A significantly enhanced vacancy concentration at the grain boundaries due to segregation, and possibly space-charge effects, could therefore account for enhanced transport along the grain boundaries. Alternatively, the distinct local structure of a grain boundary could provide a migration path with significantly lower barrier. The segregation of point defects, including oxygen vacancies, hole polarons and Sr-acceptors, to the grain boundary and/or the adjacent strained region, would influence both mechanisms.

In the present work, we provide insight into the grain boundary diffusion in LSM by means of density functional theory (DFT) calculations. The model system was chosen as the  $\Sigma 5$  (3 1 0) [0 0 1] grain boundary, which is consistent with the preferential [0 0 1] orientation of the LSM films by Navickas et al.<sup>8</sup> Polycrystalline LSM exhibits predominantly random boundaries and a slight preference for {0 0 1} grain boundary planes.<sup>12</sup> This preference may be attributed to high temperature sintering since it has been shown that SrTiO<sub>3</sub>  $\Sigma 5$  (3 1 0) [0 0 1] boundaries facet into asymmetric (0 0 1)/(4 3 0) boundaries by annealing above 1100 °C<sup>13</sup>, i.e., above the deposition temperature of the [0 0 1] oriented films.

The equilibrium stoichiometry of the grain boundary was investigated by considering segregation of oxygen vacancies and Sr-acceptors, i.e.,  $V_O^{\bullet\bullet}$  and  $Sr'_{La}$  in Kröger-Vink notation.<sup>14</sup> Furthermore, the path and barriers for oxide ion migration along the grain boundary were evaluated using the nudged elastic band (NEB) method.

## 2. Computational procedures

The DFT calculations were performed using the VASP code<sup>15</sup> and the projector-augmented wave (PAW) method<sup>16</sup>. The PBE generalized gradient approximation<sup>17</sup> was used with the DFT+*U* approach due to Dudarev et al.<sup>18</sup> An effective on-site Coulomb interaction parameter of 4.0 eV was used for Mn in line with several previous studies.<sup>19–22</sup> The plane-wave energy cut-off was 400 eV and k-point grids equivalent to  $6 \times 6 \times 6$  for the cubic LaMnO<sub>3</sub> unit cell were used. The atomic positions and cell parameters were optimized until the residual forces were within 0.02 eV Å<sup>-1</sup> (0.05 eV Å<sup>-1</sup> with point defects). The following were treated as valence states: La 5s<sup>2</sup> 5p<sup>6</sup> 5d<sup>1</sup> 6s<sup>2</sup>, Sr 4s<sup>2</sup> 5p<sup>6</sup> 6s<sup>2</sup>, Mn 3d<sup>5</sup> 4s<sup>2</sup> and O 2s<sup>2</sup> 2p<sup>4</sup>.

The ground state structure of  $\text{LaMnO}_3$  exhibits orthorhombic symmetry and Sr-doping and the elevated temperature range of interest in the present work stabilize the cubic symmetry. The LSM lattice parameter was therefore defined from a cubic  $2 \times 2 \times 2$  supercell with one Sr-substituent, corresponding to an acceptor dopant concentration of 12.5 %. The somewhat low dopant concentration was chosen since the Sr-dopant was often not explicitly included in the computational cells. The relaxed cell contained slight distortions (mainly octahedral tilting) and this optimized pseudocubic lattice parameter was used in further calculations of bulk and grain boundary cells. Ferromagnetic ordering was imposed and the magnetic moment of Mn was  $4.0 \mu_{\text{B}}$ . While LSM exhibits a thermally activated small polaron conduction mechanism at elevated temperatures,<sup>23</sup> the approach by Pavone et al.<sup>24</sup> to represent such a system by an antiferromagnetic ordering could not be appropriately relaxed in the present study. Investigation of non-ground state structures with symmetry-breaking grain boundaries and point defects are inherently challenging by these types of calculations and alternative approaches are limited at this stage.

The  $\Sigma 5 (3 1 0)[0 0 1]$  cell, hereafter  $\Sigma 5 (3 1 0)$ , was constructed with two equivalent grain boundaries separated by  $12.6 \text{ \AA}$  due to the periodic boundary conditions of the system. The atomistic structure of  $\Sigma 5 (3 1 0)$  boundaries has been optimized for similar perovskites in previous computational studies by means of rigid-body translation (RBT) and relaxation. By DFT calculations on  $\text{SrTiO}_3$  and  $\text{BaTiO}_3$ , Imaeda et al. obtained the lowest grain boundary energy for a translation of about  $4.4 \text{ \AA}$  along  $[1\bar{3}0]$  and found the resulting  $\Sigma 5 (3 1 0)$  structures to be in good agreement with high-resolution scanning transmission electron microscopy images.<sup>25</sup> Oyama et al. obtained similar results based on classical potential simulations.<sup>26</sup> Since it was determined that the optimized structure was not particularly sensitive to the initial RBT, the  $[1\bar{3}0]$  translation by Imaeda et al. was adopted in the present study and the grain separation was optimized in steps of  $0.1 \text{ \AA}$ . The grain boundary energy,  $\gamma$ , was calculated relative to a bulk cell of equivalent size and shape, according to

$$\gamma = (E_{\text{GB}}^{\text{tot}} - nE_{\text{bulk}}^{\text{tot}})/2A \quad (1)$$

where  $E_{\text{GB}}^{\text{tot}}$  and  $E_{\text{bulk}}^{\text{tot}}$  are the total energies of the grain boundary and bulk cells, respectively,  $A$  is the area of the grain boundary, and  $n$  normalized the number of  $\text{LaMnO}_3$  formula units in the cells.

The stoichiometry of  $\Sigma 5 (3 1 0)$  boundaries has been subject to some uncertainty. For  $\text{SrTiO}_3$ , Browning et al. substantiated half occupancy of the A- and B-site columns at closest proximity to each other, while Ravikumar et al. found no indications of significant cation non-stoichiometry at the interface.<sup>27,28</sup> An equivalent under-stoichiometric grain boundary model was considered in the present work by removing 2  $\text{LaMnO}_3$  formula units from the interface: La and Mn were removed alternately from columns La1/La2 and Mn2/Mn3 (see below), and oxide ions were removed by retaining an Mn-coordination number of at least 5. The optimized lattice parameter perpendicular to the boundaries was  $2 \text{ \AA}$  smaller than for the stoichiometric structure, and the relaxed structure exhibited more prominent

relaxations including splitting of the cation columns. However, as the calculated interface energy was higher than the stoichiometric structure by nearly 2 orders of magnitude, the under-stoichiometric boundary was not considered further.

Individual point defects were considered in the bulk and interface regions of supercells comprising 4 unit cells along [0 0 1] (400 atoms) sampled at the  $\Gamma$ -point. The segregation energies of the defects were obtained from the total energy difference between the grain boundary cell with the point defect residing in the bulk and interface region. Vibrational contributions to the segregation energy were not considered and it may be noted that a segregation entropy of  $2 \times 10^{-4}$  eV K<sup>-1</sup> was obtained for a  $\Sigma 3$  tilt boundary in BaZrO<sub>3</sub>.<sup>29</sup> The introduction of point defects tended to be accompanied by additional orthorhombic distortions throughout the cell and fully relaxed and distorted cells were thereby used in order to avoid contributions from these relaxations in the segregation energy. The charge state of the point defects was controlled by adding or subtracting electrons from the system, which was compensated for by a uniform background charge.

The role of space-charge on the equilibrium concentrations of point defects in the grain boundary core and adjacent regions was evaluated based on the obtained segregation energies according to a continuum space-charge model.<sup>30,31</sup> A dielectric constant of 11 was used for LSM.<sup>32</sup>

Activation barriers for migration of oxide ions were calculated using the nudged elastic band method (NEB). These barriers correspond to relaxed static barriers, i.e., the surrounding lattice is able to relax instantaneously around the oxide ion throughout the migration event. These relaxed configurations can be expected to be close to those observed during migration in a dynamic simulation. NEB calculations were performed by relaxation of the nearest neighbour La ions and Mn-octahedra in the pseudocubic tilted cells, and with full relaxation in the orthorhombic distorted cells. The ionic charge of the migrating oxide ions were evaluated by Bader charge analysis.<sup>33</sup>

## 3. Results

### 3.1 Grain boundary structure

Figure 1 shows the relaxed structure of the LaMnO<sub>3</sub>  $\Sigma 5$  (3 1 0) grain boundary. The optimized cell size corresponded to an expansion of 1.36 Å perpendicular to each of the two equivalent boundaries in the computational cell (7.79 Å × 12.31 Å × 26.74 Å). The presence of grain boundaries induced orthorhombic distortion throughout the pseudocubic structure, which did not occur for a bulk cell of similar size and shape. For this reason, the calculated grain boundary energy was not well defined due to contributions from orthorhombic relaxation. Nevertheless, a value of 0.29 J m<sup>-2</sup> was obtained, indicative of a stable structure. In comparison, grain boundary energies in the range 0.3-1.4 J m<sup>-2</sup> were reported for  $\Sigma 3$  and  $\Sigma 5$  boundaries in perovskite SrTiO<sub>3</sub>, BaTiO<sub>3</sub>, BaZrO<sub>3</sub> and PbZrO<sub>3</sub>.<sup>25,31,34-36</sup>

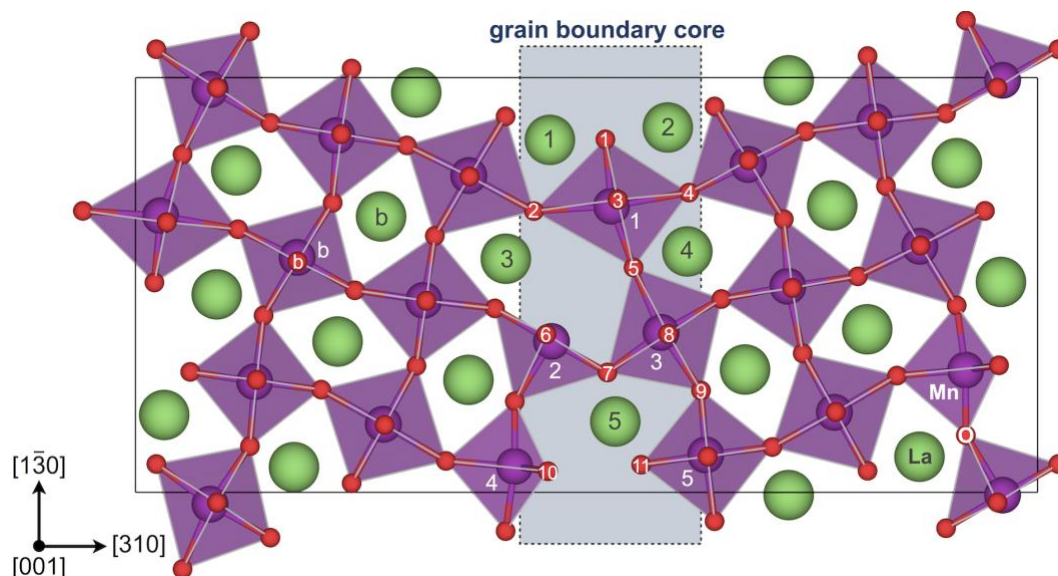


Figure 1: Relaxed structure of the pseudocubic  $\text{LaMnO}_3 \Sigma 5 (3\ 1\ 0)$  grain boundary. Segregation of point defects was considered for the numbered sites in the core region relative to the sites in the bulk region (b).

### 3.2 Point defect segregation

The calculated segregation energies of for  $V_{\text{O}}^{\bullet\bullet}$  and  $\text{Sr}'_{\text{La}}$  are summarized in Table 1. There is a considerable tendency for oxygen vacancies to segregate to the grain boundary core, especially to sites O1, O3 and O11 (see Figure 1). Sr also exhibits quite a strong tendency to segregate to the La1 site with a segregation energy of -0.43 eV.

Table 1: Defect segregation energies of oxygen vacancies and Sr-acceptors to the grain boundary core sites defined in Figure 1, as well as oxygen vacancy segregation energies in the presence of a Sr-acceptor on La1 site.

Oxygen vacancy	$\Delta E_i^{\text{seg}} / \text{eV}$	Sr-acceptor	$\Delta E_i^{\text{seg}} / \text{eV}$
$V_{\text{O},1}^{\bullet\bullet}$	-0.33	$\text{Sr}'_{\text{La},1}$	-0.43
$V_{\text{O},2}^{\bullet\bullet}$	0.18	$\text{Sr}'_{\text{La},2}$	-0.09
$V_{\text{O},3}^{\bullet\bullet}$	-0.59	$\text{Sr}'_{\text{La},3}$	-0.09
$V_{\text{O},4}^{\bullet\bullet}$	0.16	$\text{Sr}'_{\text{La},4}$	0.08
$V_{\text{O},5}^{\bullet\bullet}$	-0.02	$\text{Sr}'_{\text{La},5}$	0.08
$V_{\text{O},6}^{\bullet\bullet}$	-0.14		
$V_{\text{O},7}^{\bullet\bullet}$	0.68		
$V_{\text{O},8}^{\bullet\bullet}$	-0.20		
$V_{\text{O},9}^{\bullet\bullet}$	-0.18	<b>Oxygen vacancy w/<math>\text{Sr}'_{\text{La},1}</math></b>	
$V_{\text{O},10}^{\bullet\bullet}$	0.61	$V_{\text{O},1}^{\bullet\bullet}$	-0.37
$V_{\text{O},11}^{\bullet\bullet}$	-0.82	$V_{\text{O},11}^{\bullet\bullet}$	-0.35

In the case of  $V_{\text{O},11}^{\bullet\bullet}$ , the lowest energy configuration was obtained by displacement of the adjacent oxide ion by half a unit cell along  $[0\ 0\ 1]$ . The relaxed structure, shown in Figure 2, contains an oxide ion residing within a trigonal configuration of  $\text{La}^{3+}$  and the calculated segregation energy was -0.82 eV. It was confirmed that this oxide ion position was favorable only adjacent to  $V_{\text{O},11}^{\bullet\bullet}$  since the configuration with displacement of all three  $\text{O}_{\text{O},11}^{\times}$  was less stable by 0.76 eV. The  $V_{\text{O},11}^{\bullet\bullet}$  defect could also be stabilized in the pseudocubic cell without introducing orthorhombic distortions. The calculated segregation energy was -1.06 eV, and displacement of the adjacent oxide ion was not found to be favoured in this

case. The strong tendency for vacancy segregation to the O11 site may be ascribed to its singly coordinated nature compared to the nominal 2-fold coordination for corner sharing octahedra (Figure 1). On the other hand, the unfavourable segregation energy to the O7 and O10 sites may be associated with the 5-fold coordination of Mn2 and Mn4, although vacancy segregation to O6 (bound to Mn2) was slightly favourable.

Oxygen vacancy segregation energies were also calculated in the presence of the most favourable Sr-acceptor,  $\text{Sr}'_{\text{La},1}$ . The segregation energy for vacancies to O1 was quite similar in the presence of  $\text{Sr}'_{\text{La},1}$ ,  $-0.37$  eV compared to  $-0.33$  eV (Table 1). On the other hand, the segregation energy to O11 was significantly less exothermic with a nearest neighbour  $\text{Sr}'_{\text{La},1}$ ,  $-0.35$  eV.

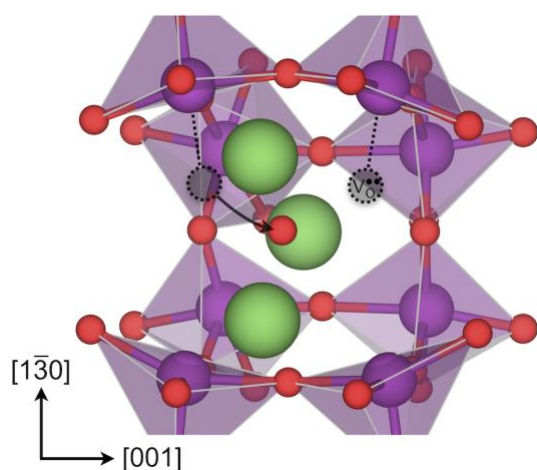


Figure 2: Fully relaxed structure of  $V_{\text{O},11}^{..}$  where the adjacent oxide ion was displaced (arrow) from its initial position (gray sphere).

### 3.3 Defect concentration profiles

Based on the segregation energies in Table 1, the concentrations of point defects were calculated for the grain boundary core and adjacent space-charge regions. Figure 3 shows the concentration and potential profile at 873 K for a bulk oxygen vacancy concentration of  $\delta=5 \times 10^{-7}$ . The core attained a slight positive charge due to the favorable segregation of oxygen vacancies. A low core potential of 5 mV was obtained due to the high Sr-dopant concentration and corresponding high bulk concentrations of electron holes that deplete in the space-charge region to compensate the core charge. Nevertheless, the enhancement in core oxygen vacancy concentration was large at nearly 4 orders of magnitude with about  $\delta=1.1 \times 10^{-2}$  ascribed to  $V_{\text{O},11}^{..}$ . Notably, the depletion of oxygen vacancies in the space-charge region was quite insignificant.

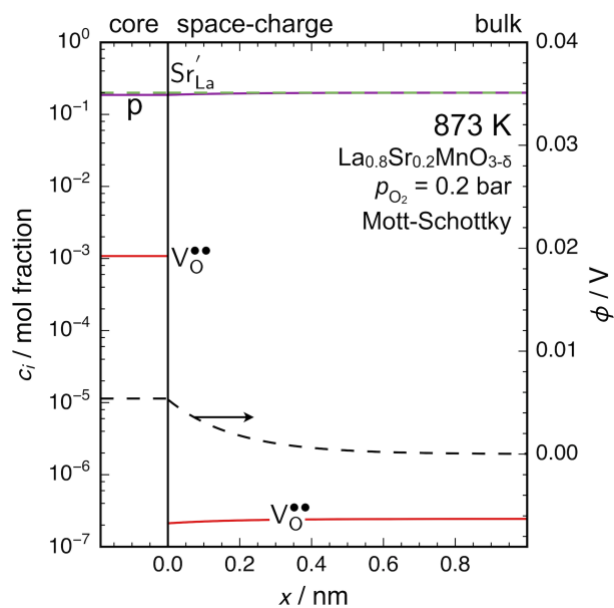


Figure 3: Point defect concentration and potential profiles in the grain boundary core the adjacent space-charge region.

### 3.4 Migration pathways

Potentially fast oxide ion migration paths along the core were evaluated based on the calculated vacancy concentrations and the interconnectivity between the sites. In this respect, site O11 exhibited both the highest vacancy concentration and direct connectivity between adjacent O11 sites along  $[0\ 0\ 1]$ . Another potentially important migration path was identified between sites O1 and O3 that forms an intraoctahedral path along  $[0\ 0\ 1]$ . The O1 and O3 sites also exhibited relatively high vacancy concentrations.

Figure 4 shows the migration path and corresponding energy barrier for oxide ion migration between adjacent O11 sites in the pseudocubic cell. The calculated migration barrier amounts to 0.51 eV and exhibits a slightly metastable state midway along the path. The bond lengths in Figure 4b show that the migrating oxide ion retains its bond to La throughout the migration event, while it is not bound to Mn for about 2 Å midway through the migration. A similar activation barrier of 0.52 eV was obtained for the orthorhombic distorted cell with the initial and final positions similar to that in Figure 2. In the presence of  $\text{Sr}'_{\text{La}}$  segregated to the most favourable La1 site, the barrier increased to 0.58 eV for migration past and away from  $\text{Sr}'_{\text{La}}$  (Figure 4b).

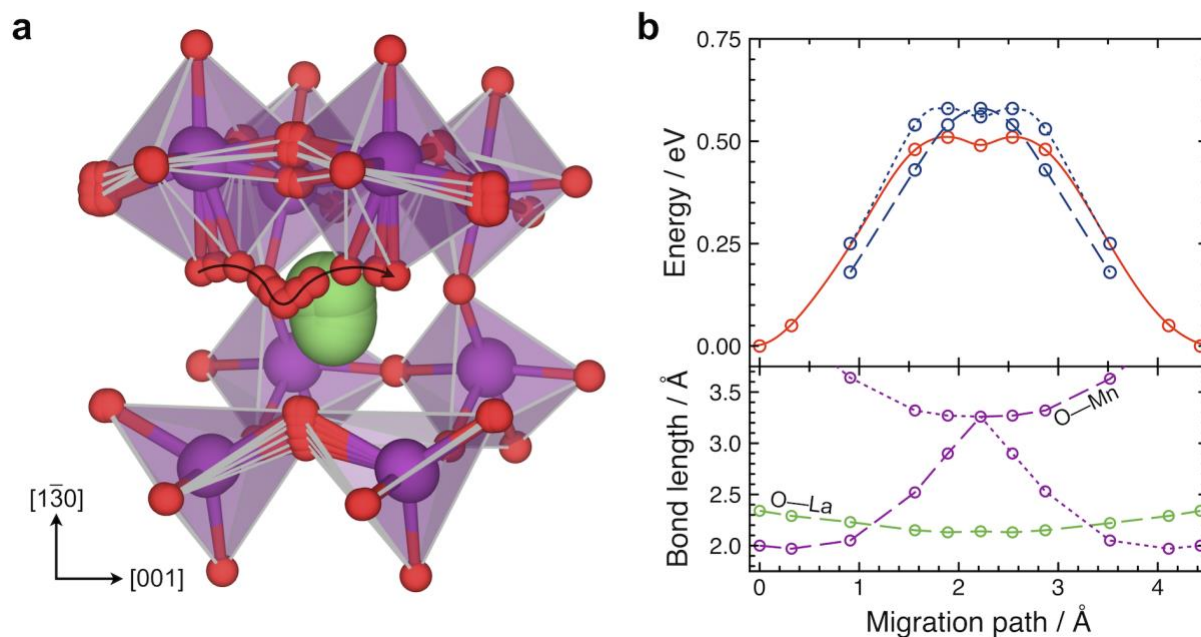


Figure 4: Migration path for oxide ions through  $V_{O,11}^{**}$  along  $[0\ 0\ 1]$  (a) and the corresponding energy profile and bond lengths throughout the migration event (b). The dashed and dotted energy profiles represent migration away from and past  $Sr'_{La1}$ , respectively.

The path and barrier for intraoctahedral migration from O1 to O3 sites in the distorted cell is shown in Figure 5. The overall barrier amounts to 0.59 eV and is asymmetric in accordance with the difference in oxygen vacancy stability on the O1 and O3 sites (Table 1). The bond length to Mn is rather constant throughout the migration event, and there is a slight reduction in the distance to the two nearest La-ions (Figure 5b). Both migration barriers are lower than the bulk value of 0.64-0.69 eV obtained with similar calculations for  $LaMnO_3$ .<sup>37,38</sup> The ionic charge of the migrating oxide ion was essentially unchanged during migration with an increase of  $0.02e$  at the transition state for both paths. On the contrary, similar studies on  $Ba_{1-x}Sr_xCo_{1-y}Fe_yO_{2.875}$  showed a slight decrease in the charge of the migrating oxide ion of about  $0.1e$ .<sup>39</sup>

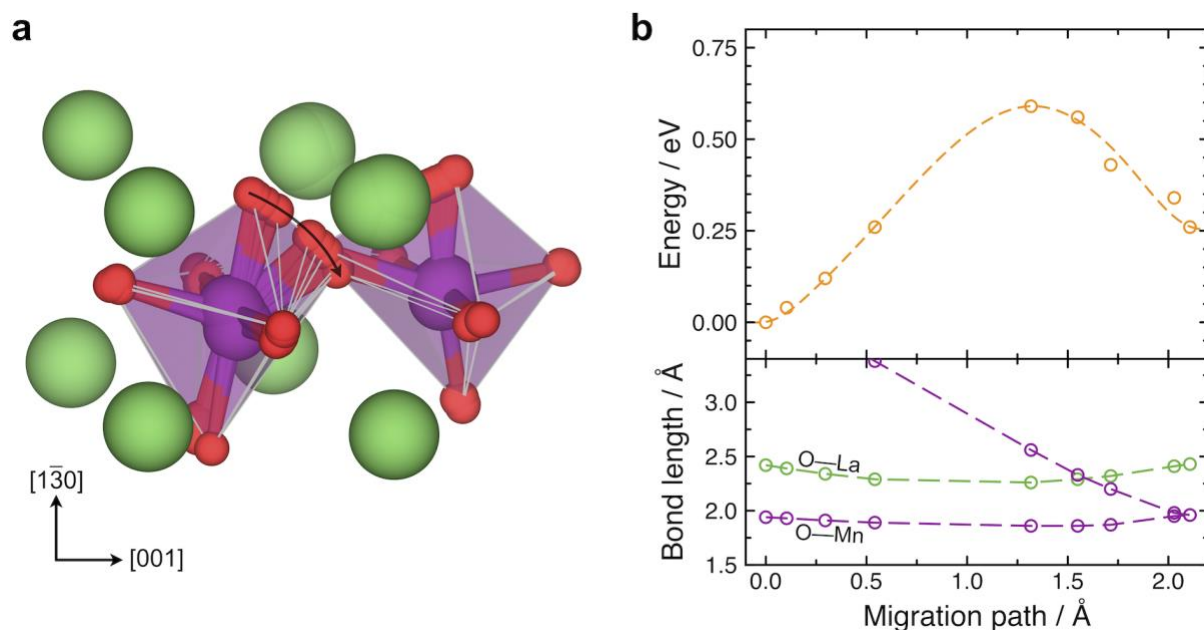


Figure 5: Migration path for oxide ions from O3 to O1 along [0 0 1] (a) and the corresponding energy profile and bond lengths throughout the migration event (b).

#### 4. Discussion

Fast grain boundary diffusion in doped systems can in general be ascribed to enhanced defect concentrations in space-charge regions, or enhanced mobility and/or defect concentration in the grain boundary core.<sup>40</sup> Increased concentrations of  $V_{O}^{\bullet\bullet}$  in space-charge regions necessitates a negatively charged core which could potentially arise in LSM due to significant segregation of  $Sr'_{La}$ . Nevertheless, significant enhancement in the concentration of a minority defect such as  $V_{O}^{\bullet\bullet}$  is not possible in such a heavily doped material with a mobile majority defect, i.e., electron holes. As seen in the obtained potential and concentration profiles in Figure 3, slight changes in the concentration of the electron holes in the space-charge regions compensated the core charge, resulting in a minute change in  $V_{O}^{\bullet\bullet}$  concentrations in the space-charge regions. On the other hand, the oxygen vacancy concentration in the core increased by several orders of magnitude.

The diffusivity along the grain boundary core relative to the bulk can be evaluated according to the concentration enhancement and enthalpies of mobility related to the O1+O3 path and the O11 path. The diffusion coefficient for oxide ions can be expressed as

$$D = D_0 \exp\left(-\frac{\Delta H_f + \Delta H_m}{kT}\right) \quad (2)$$

where  $\Delta H_f$  is the enthalpy of defect formation and  $\Delta H_m$  is the enthalpy of mobility. The pre-exponential factor  $D_0$  includes the entropy of defect formation as well parameters related to the structure, symmetry and vibrational properties of the diffusing species. For the considered migration paths,  $D_0$  can reasonably be assumed to be rather similar to that in the bulk due to the basic similarity in the local structural environment comprising Mn-octahedra.

The formation of oxygen vacancies in the intermediate  $p_{O_2}$ -range can be described according to the consumption of holes



The enthalpy of vacancy formation was taken as 2.0 eV based on values deduced from tracer diffusion measurements under similar conditions.<sup>41,42</sup> It should be noted that values of up to 3.14 eV have been reported based on significantly larger ranges in  $p_{\text{O}_2}$  and different doping concentrations.<sup>43–45</sup> The bulk oxygen vacancy concentration was obtained from the equilibrium constant of Reaction 3 according to

$$c_{V_{\text{O},b}} = \frac{3}{V} p^2 p_{\text{O}_2}^{\frac{1}{2}} \exp\left(-\frac{\Delta H_{f,b}}{kT}\right) \exp\left(\frac{\Delta S_{f,b}}{k}\right) \quad (4)$$

with a simplified electroneutrality condition of  $p = c_{\text{Sr}'_{\text{La}}}$  and a site density of 3 per pseudocubic unit cell volume,  $V$ . The entropy of Reaction 3,  $\Delta S_{f,b}$ , was estimated to 1.2 meV/K based on thermochemical data of the gaseous species,  $\frac{1}{2}\text{O}_2(\text{g})$ .<sup>46</sup> Figure 6a shows bulk oxygen vacancy concentration and the corresponding enhancement in the core concentrations estimated based on the segregation energies in Table 1, i.e., assuming local electroneutrality due to the insignificant core potentials (Figure 3). The variation in core concentration with inverse temperature yields an apparent  $\Delta H_{f,gb}$  of 1.0-1.4 eV. A lower limit  $V_{\text{O},11}^{\bullet\bullet}$  concentration is also shown as a dashed line based on the segregation energy to O11 sites with nearest neighbour  $\text{Sr}'_{\text{La}1}$ , i.e., -0.35 eV (Table 1). This lower limit can be expected to be less relevant since it would correspond to a  $\text{Sr}'_{\text{La}1}$  concentration close to saturation, and because  $V_{\text{O},11}^{\bullet\bullet}$  and  $\text{Sr}'_{\text{La}1}$  would compete for the same sites (noting the more exothermic segregation energy of  $V_{\text{O},11}^{\bullet\bullet}$  compared to  $\text{Sr}'_{\text{La}1}$ ). In terms of long-range oxide ion migration, the O11 sites adjacent to  $\text{Sr}'_{\text{La}1}$  can be considered metastable at a relative energy lower than the migration barrier.

The enhancement in grain boundary diffusion relative to bulk is illustrated in Figure 6b with a bulk enthalpy of mobility of 0.70 eV (Table 2).<sup>47</sup> The O11 path predominates the total oxygen diffusion along the core which is about 3 to 5 orders of magnitude higher than bulk. The estimated enhancement in grain boundary diffusivity for the  $\Sigma 5$  (3 1 0) boundary lies in the same range as the 3 to 6 orders of magnitude reported for PLD films.<sup>8,9</sup> Furthermore, the estimated activation energies for grain boundary diffusion, 1.6-2.0 eV, correspond quite well with those obtained for columnar and (0 0 1) oriented PLD films, 1.8-2.2 eV.<sup>8,9</sup> For comparison, the reported activation energies for bulk diffusion as well as grain boundary diffusion in a polycrystalline sample were somewhat larger, 2.6-2.8 eV and 3.1 eV, respectively.<sup>8,41</sup>

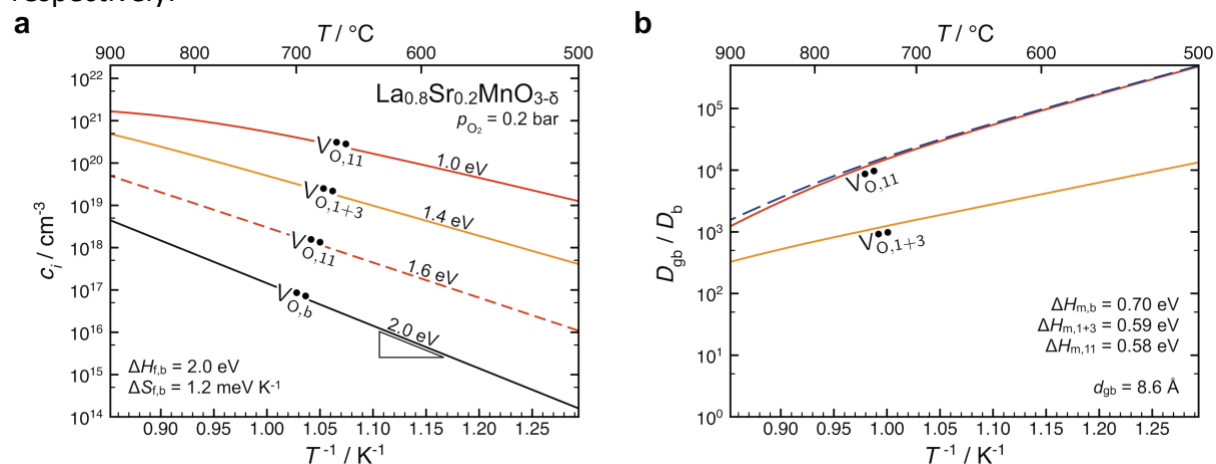


Figure 6: Oxygen vacancy concentrations in bulk and the predominating core sites (a) and the ratio between bulk and grain boundary diffusivity with contribution from the O1+O3 and O11 paths (b) as function of inverse temperature. The dashed line in a) corresponds to the lower limit O11 vacancy concentration based on segregation to sites neighboring  $\text{Sr}'_{\text{La}1}$ .

Table 2: Summary of the parameters involved in estimating diffusion along the O1+O3 and O11 paths as well as reference values for bulk. The concentrations and diffusion coefficient ratios were obtained for 700 °C and  $p_{O_2}=0.2$  bar.

Path	O1+O3	O11	bulk
$E_{V_O^{\bullet\bullet}}^{seg} / \text{eV}$	-0.33 / -0.59	-0.82	-
$\Delta H_f / \text{eV}$	1.4	1.0	2.0 <sup>41,42</sup>
$\Delta H_m / \text{eV}$	0.59	0.58	0.70 <sup>47</sup>
$c_{V_O^{\bullet\bullet}} / \text{cm}^{-3}$	$3.2 \times 10^{19}$	$4.0 \times 10^{20}$	$7.6 \times 10^{16}$
$D_{gb}/D_b$	$1.6 \times 10^3$	$2.2 \times 10^4$	-

The general applicability of the present results to other material systems can be evaluated based on their bulk and grain boundary properties. In this respect, similar grain boundary structures and oxygen vacancy segregation energies have been reported for several perovskites including SrTiO<sub>3</sub>, BaTiO<sub>3</sub>, BaZrO<sub>3</sub> and BaCeO<sub>3</sub>.<sup>25,26,36,48–51</sup> The grain boundary oxygen vacancy diffusivity may therefore be comparable to that in LSM for these materials. However, in contrast to LSM, these oxides exhibit significant oxygen vacancy concentrations in the bulk when acceptor doped. Thus, the relative contribution from the grain boundary to the overall oxygen vacancy diffusivity becomes minor in these systems. The prospect of enhanced grain boundary vacancy diffusion in acceptor doped perovskites can therefore be expected to largely depend on the bulk oxygen vacancy concentration as determined by the enthalpy of Reaction 3. The grain size or grain boundary density will also influence the contribution from grain boundaries to the overall oxygen vacancy diffusivity.

Donor-doped perovskites exhibit low bulk oxygen vacancy concentrations and may as such exhibit similar grain boundary properties as LSM. Indeed, significantly enhanced grain boundary diffusivities have been reported in donor-doped BaTiO<sub>3</sub> and PbZrO<sub>3</sub> in tracer diffusion and conductivity relaxation studies.<sup>52–54</sup> In these donor-doped systems, oxygen vacancies may form according to the reduction reaction



Oxygen vacancies may also be partly charge compensated by cation vacancies introduced during sample preparation, e.g.,  $V_{Ba}''$  or  $V_{Pb}''$ , but remain a minority defect under most conditions.<sup>55</sup> Donor-doped BaTiO<sub>3</sub> ceramics exhibit a negative core charge that is usually associated with a frozen-in segregation profile of cation vacancies at the grain boundaries.<sup>56</sup> Furthermore, the considerable core potentials result in significant depletion of electrons and accumulation of oxygen vacancies in the space-charge regions, in contrast to LSM as discussed in Section 4. Thus, fast grain boundary diffusion due to space-charge is reasonable in donor-doped perovskites with negatively charged grain boundary cores. A negatively charged core does, however, not exclude segregation of minority oxygen vacancies as long as the concentration is lower than the effectively negatively charged defects. Diffusion along the core may therefore contribute to the enhanced grain boundary diffusion as long as the structure contains interconnected diffusion paths between the oxygen vacancy sites in the core.

## 5. Conclusions

LSM grain boundaries with similar properties as  $\Sigma 5$  (3 1 0)[0 0 1] with respect to stabilization of oxygen vacancies can explain the fast oxide ion diffusion observed in tracer diffusion measurements. The estimated diffusion coefficient along the grain boundary core was about 3 to 5 orders of magnitude higher than bulk in the range 500-900 °C. The enhanced grain boundary diffusion originated from significantly higher concentrations of oxygen vacancies at core sites, interconnected through long-range diffusion paths. The obtained results comply with the general tendency for grain boundaries to act as barriers for fast species, while they can act as fast paths for species that otherwise exhibit slow diffusivity in the bulk.

## 6. Acknowledgements

The authors acknowledge financial support from the Research Council of Norway through the Nano2021 program and FOX CET project (228355). Computational resources were provided through the Norwegian Metacenter for Computational Science (NOTUR) under the project nn9259k. Yildiz and Tuller acknowledge support for their research from the Department of Energy, Basic Energy Sciences under award number DE-SC0002633 (Chemomechanics of Far-From-Equilibrium Interfaces).

## 7. References

- 1 J. A. Kilner and M. Burriel, Materials for Intermediate-Temperature Solid-Oxide Fuel Cells, *Annu. Rev. Mater. Res.*, 2014, **44**, 365–393.
- 2 A.-M. Haghiri-Gosnet and J.-P. Renard, CMR manganites: physics, thin films and devices, *J. Phys. D: Appl. Phys.*, 2003, **36**, R127–R150.
- 3 S. P. Jiang, Development of lanthanum strontium manganite perovskite cathode materials of solid oxide fuel cells: a review, *J. Mater. Sci.*, 2008, **43**, 6799–6833.
- 4 M. Juhl, S. Primdahl, C. Manon and M. Mogensen, Performance/structure correlation for composite SOFC cathodes, *J. Power Sources*, 1996, **61**, 173–181.
- 5 J. Nielsen and J. Hjelm, Impedance of SOFC electrodes: A review and a comprehensive case study on the impedance of LSM:YSZ cathodes, *Electrochim. Acta*, 2014, **115**, 31–45.
- 6 L. C. Baque, P. S. Jorgensen, K. V. Hansen and M. Sogaard, Long-Term Stability of LSM-YSZ Based Cathodes, *ECS Trans.*, 2013, **57**, 2027–2036.
- 7 Q. Su, D. Yoon, Z. Sisman, F. Khatkhatay, Q. Jia, A. Manthiram and H. Wang, Vertically aligned nanocomposite  $\text{La}_{0.8}\text{Sr}_{0.2}\text{MnO}_{3-\delta}/\text{Zr}_{0.92}\text{Y}_{0.08}\text{O}_{1.96}$  thin films as electrode/electrolyte interfacial layer for solid oxide reversible fuel cells, *Int. J. Hydrogen Energy*, 2013, **38**, 16320–16327.
- 8 E. Navickas, T. M. Huber, Y. Chen, W. Hetaba, G. Holzlechner, G. Rupp, M. Stöger-Pollach, G. Friedbacher, H. Hutter, B. Yildiz and J. Fleig, Fast oxygen exchange and diffusion kinetics of grain boundaries in Sr-doped  $\text{LaMnO}_3$  thin films, *Phys. Chem. Chem. Phys.*, 2015, **17**, 7659–7669.
- 9 A. M. Saranya, D. Pla, A. Morata, A. Cavallaro, J. Canales-Vázquez, J. A. Kilner, M. Burriel and A. Tarancón, Engineering mixed ionic electronic conduction in  $\text{La}_{0.8}\text{Sr}_{0.2}\text{MnO}_{3+\delta}$  nanostructures through fast grain boundary oxygen diffusivity, *Adv. Energy Mater.*, 2015, **5**, 1–6.
- 10 E. Navickas, Y. Chen, Q. Lu, W. Wallisch, T. M. Huber, J. Bernardi, M. Stöger-Pollach, G. Friedbacher, H. Hutter, B. Yildiz and J. Fleig, Dislocations Accelerate Oxygen Ion Diffusion in  $\text{La}_{0.8}\text{Sr}_{0.2}\text{MnO}_3$  Epitaxial Thin Films, *ACS Nano*, 2017, acsnano.7b06228.
- 11 G. Gregori, R. Merkle and J. Maier, Ion conduction and redistribution at grain boundaries in oxide systems, *Prog. Mater. Sci.*, 2017, **89**, 252–305.

- 12 Q. Liu, S. Bhattacharya, L. Helmick, S. P. Donegan, A. D. Rollett, G. S. Rohrer and P. A. Salvador, Crystallography of Interfaces and Grain Size Distributions in Sr-Doped LaMnO<sub>3</sub>, *J. Am. Ceram. Soc.*, 2014, **97**, 2623–2630.
- 13 S. B. Lee, W. Sigle, W. Kurtz and M. Rühle, Temperature dependence of faceting in  $\Sigma(310)[001]$  grain boundary of SrTiO<sub>3</sub>, *Acta Mater.*, 2003, **51**, 975–981.
- 14 F. A. Kröger and H. J. Vink, Relations between the Concentrations of Imperfections in Crystalline Solids, *Solid State Phys.*, 1956, **3**, 307–435.
- 15 G. Kresse and D. Joubert, From ultrasoft pseudopotentials to the projector augmented-wave method, *Phys. Rev. B*, 1999, **59**, 1758–1775.
- 16 P. E. Blöchl, Projector augmented-wave method, *Phys. Rev. B*, 1994, **50**, 17953–17979.
- 17 J. Perdew, K. Burke and M. Ernzerhof, Generalized Gradient Approximation Made Simple., *Phys. Rev. Lett.*, 1996, **77**, 3865–3868.
- 18 S. L. Dudarev, S. Y. Savrasov, C. J. Humphreys and A. P. Sutton, Electron-energy-loss spectra and the structural stability of nickel oxide: An LSDA+U study, *Phys. Rev. B*, 1998, **57**, 1505–1509.
- 19 Y. L. Lee, J. Kleis, J. Rossmeisl and D. Morgan, Ab initio energetics of LaBO<sub>3</sub> (001) (B=Mn, Fe, Co, and Ni) for solid oxide fuel cell cathodes, *Phys. Rev. B - Condens. Matter Mater. Phys.*, 2009, **80**, 1–20.
- 20 H. Jalili, J. W. Han, Y. Kuru, Z. Cai and B. Yildiz, New insights into the strain coupling to surface chemistry, electronic structure, and reactivity of La<sub>0.7</sub>Sr<sub>0.3</sub>MnO<sub>3</sub>, *J. Phys. Chem. Lett.*, 2011, **2**, 801–807.
- 21 W. Lee, J. W. Han, Y. Chen, Z. Cai and B. Yildiz, Cation size mismatch and charge interactions drive dopant segregation at the surfaces of manganite perovskites, *J. Am. Chem. Soc.*, 2013, **135**, 7909–7925.
- 22 Y. Wang and H.-P. Cheng, Oxygen Reduction Activity on Perovskite Oxide Surfaces: A Comparative First-Principles Study of LaMnO<sub>3</sub>, LaFeO<sub>3</sub> and LaCrO<sub>3</sub>, *J. Phys. Chem. C*, 2013, 130110122700005.
- 23 J. P. P. H. and L. P. J.A, M. van Roosmalen, Electrical conductivity in La<sub>1-x</sub>Sr<sub>x</sub>MnO<sub>3+δ</sub>, *Solid State Ionics*, 1993, **66**, 279–284.
- 24 M. Pavone, A. M. Ritzmann and E. A. Carter, Quantum-mechanics-based design principles for solid oxide fuel cell cathode materials, *Energy Environ. Sci.*, 2011, **4**, 4933.
- 25 M. Imaeda, T. Mizoguchi, Y. Sato, H. S. Lee, S. D. Findlay, N. Shibata, T. Yamamoto and Y. Ikuhara, Atomic structure, electronic structure, and defect energetics in [001](310) $\Sigma$  grain boundaries of SrTiO<sub>3</sub> and BaTiO<sub>3</sub>, *Phys. Rev. B - Condens. Matter Mater. Phys.*, 2008, **78**, 1–12.
- 26 T. Oyama, N. Wada, H. Takagi and M. Yoshiya, Trapping of oxygen vacancy at grain boundary and its correlation with local atomic configuration and resultant excess energy in barium titanate: A systematic computational analysis, *Phys. Rev. B - Condens. Matter Mater. Phys.*, 2010, **82**, 1–10.
- 27 N. D. Browning, S. J. Pennycook, M. F. Chisholm, M. M. McGibbon and A. J. McGibbon, Observation of structural units at symmetric [001] tilt boundaries in SrTiO<sub>3</sub>, *Interface Sci.*, 1995, **2**, 397–423.
- 28 V. Ravikumar and V. P. Dravid, Atomic structure of undoped  $\Sigma = 5$  symmetrical tilt grain boundary in strontium titanate, *Ultramicroscopy*, 1993, **52**, 557–563.
- 29 A. Lindman, T. S. Bjørheim and G. Wahnström, Defect segregation to grain boundaries in BaZrO<sub>3</sub> from first-principles free energy calculations, *J. Mater. Chem. A*, 2017, **5**, 13421–13429.
- 30 K. L. Kliewer and J. S. Koehler, Space Charge in Ionic Crystals. I. General Approach with Application to NaCl, *Phys. Rev.*, 1965, **140**, A1226.
- 31 J. M. Polfus, K. Toyoura, F. Oba, I. Tanaka and R. Haugsrud, Defect chemistry of a BaZrO<sub>3</sub>  $\Sigma 3$  (111) grain boundary by first principles calculations and space-charge theory., *Phys. Chem. Chem. Phys.*, 2012, **14**, 12339–46.
- 32 A. O. Turky, M. M. Rashad, A. M. Hassan, E. M. Elnaggar and M. Bechelany, Tailoring optical, magnetic and electric behavior of lanthanum strontium manganite La<sub>1-x</sub>Sr<sub>x</sub>MnO<sub>3</sub> (LSM) nanopowders prepared via a co-precipitation method with different Sr<sup>2+</sup> ion contents, *RSC Adv.*, 2016, **6**, 17980–17986.
- 33 W. Tang, E. Sanville and G. Henkelman, A grid-based Bader analysis algorithm without lattice bias., *J.*

- Phys. Condens. Matter*, 2009, **21**, 084204.
- 34 S. Hutt, Köstlmeier and C. Elsässer, Density functional study of the  $\Sigma$ 3 (111) [1 1 0] symmetrical tilt grain boundary in SrTiO<sub>3</sub>, *J. Phys. Condens. Matter*, 2001, **13**, 3949–3960.
- 35 P. Marton, T. Shimada, T. Kitamura and C. Elsässer, First-principles study of the interplay between grain boundaries and domain walls in ferroelectric PbTiO<sub>3</sub>, *Phys. Rev. B - Condens. Matter Mater. Phys.*, 2011, **83**, 064110, DOI:10.1103/PhysRevB.83.064110.
- 36 E. E. Helgee, A. Lindman and G. Wahnström, Origin of Space Charge in Grain Boundaries of Proton-Conducting BaZrO<sub>3</sub>, *Fuel Cells*, 2013, **13**, 19–28.
- 37 H. Kwon, J. Park, B. Kim, J. W. Han, H. Temperature and E. Materials, Effect of B-cation doping on oxygen vacancy formation and migration in LaBO<sub>3</sub>: A density functional theory study, *J. Korean Ceram. Soc.*, 2015, **52**, 331–337.
- 38 T. Mayeshiba and D. Morgan, Strain effects on oxygen migration in perovskites, *Phys. Chem. Chem. Phys.*, 2015, **17**, 2715–2721.
- 39 R. Merkle, Y. A. Mastrikov, E. A. Kotomin, M. M. Kuklja and J. Maier, First Principles Calculations of Oxygen Vacancy Formation and Migration in Ba<sub>1-x</sub>Sr<sub>x</sub>Co<sub>1-y</sub>Fe<sub>y</sub>O<sub>3-δ</sub> Perovskites, *J. Electrochem. Soc.*, , DOI:10.1149/2.077202jes.
- 40 J. Maier, Defect chemistry and ion transport in nanostructured materials: Part II. Aspects of nanoionics, *Solid State Ionics*, 2003, **157**, 327–334.
- 41 R. A. De Souza, J. A. Kilner and J. F. Walker, SIMS study of oxygen tracer diffusion and surface exchange in La<sub>0.8</sub>Sr<sub>0.2</sub>MnO<sub>3+δ</sub>, *Mater. Lett.*, 2000, **43**, 43–52.
- 42 S. Fearn, J. C. H. Rossiny, J. A. Kilner and J. R. G. Evans, Measurement of oxygen transport in La<sub>0.8</sub>Sr<sub>0.2</sub>MnO<sub>3</sub> perovskite grains, *Solid State Ionics*, 2012, **211**, 51–57.
- 43 J. Nowotny and M. Rekas, Defect Chemistry of (La,Sr)MnO<sub>3</sub>, *J. Am. Ceram. Soc.*, 1998, **81**, 67–80.
- 44 S. Tanasescu, C. Marinescu, F. Maxim, A. Sofronia and N. Totir, Evaluation of manganese and oxygen content in La<sub>0.7</sub>Sr<sub>0.3</sub>MnO<sub>3-δ</sub> and correlation with the thermodynamic data, *J. Solid State Electrochem.*, 2011, **15**, 189–196.
- 45 M. Takacs, M. Hoes, M. Caduff, T. Cooper, J. R. Scheffe and A. Steinfeld, Oxygen nonstoichiometry, defect equilibria, and thermodynamic characterization of LaMnO<sub>3</sub> perovskites with Ca/Sr A-site and Al B-site doping, *Acta Mater.*, 2016, **103**, 700–710.
- 46 M. Chase, NIST-JANAF Thermochemical Tables, 4th Edition, *J. Phys. Chem. Ref. Data*, 1998, **Monograph**, 1952.
- 47 M. S. Islam, M. Cherry and C. R. A. Catlow, Oxygen Diffusion in LaMnO<sub>3</sub> and LaCoO<sub>3</sub> Perovskite-Type Oxides: A Molecular Dynamics Study, *J. Solid State Chem.*, 1996, **124**, 230–237.
- 48 B. P. Uberuaga, S. Choudhury, X.-M. Bai and N. A. Benedek, Grain boundary stoichiometry and interactions with defects in SrTiO<sub>3</sub>, *Scr. Mater.*, 2012, **66**, 105–108.
- 49 R. Astala and P. D. Bristowe, A computational study of twist boundary structures in strontium titanate, *J. Phys. Condens. Matter*, 2002, **14**, 13635–13641.
- 50 T. Tauer, R. O’Hayre and J. W. Medlin, Computational investigation of defect segregation at the (001) surface of BaCeO<sub>3</sub> and BaZrO<sub>3</sub>: the role of metal-oxygen bond strength in controlling vacancy segregation, *J. Mater. Chem. A*, 2013, **1**, 2840–2846.
- 51 J. M. Polfus, M. Pishahang and R. Bredesen, Influence of Ce<sup>3+</sup> polarons on grain boundary space-charge in proton conducting Y-doped BaCeO<sub>3</sub>, *Phys. Chem. Chem. Phys.*, 2018, **20**, 16209–16215.
- 52 T. Frömling, J. Hou, W. Preis, W. Sitte, H. Hutter and J. Fleig, Oxygen tracer diffusion in donor doped barium titanate, *J. Appl. Phys.*, 2011, **110**, 043531.
- 53 W. Preis, Chemical diffusion and defect chemistry of grain boundaries in n-type barium titanate ceramics, *Solid State Ionics*, 2017, **299**, 82–88.
- 54 T. Frömling, A. Schintlmeister, H. Hutter and J. Fleig, Oxide Ion Transport in Donor-Doped Pb(Zr<sub>x</sub>Ti<sub>1-x</sub>)O<sub>3</sub>: The Role of Grain Boundaries, *J. Am. Ceram. Soc.*, 2011, **94**, 1173–1181.

- 55 T. Shi, Y. Chen and X. Guo, Defect chemistry of alkaline earth metal (Sr/Ba) titanates, *Prog. Mater. Sci.*, 2016, **80**, 77–132.
- 56 W. Preis and W. Sitte, Modelling of grain boundary resistivities of n-conducting BaTiO<sub>3</sub> ceramics, *Solid State Ionics*, 2006, **177**, 2549–2553.